Volume 5
Number 9
7 May 2024
Pages 3521–4008

Materials Advances

rsc.li/materials-advances

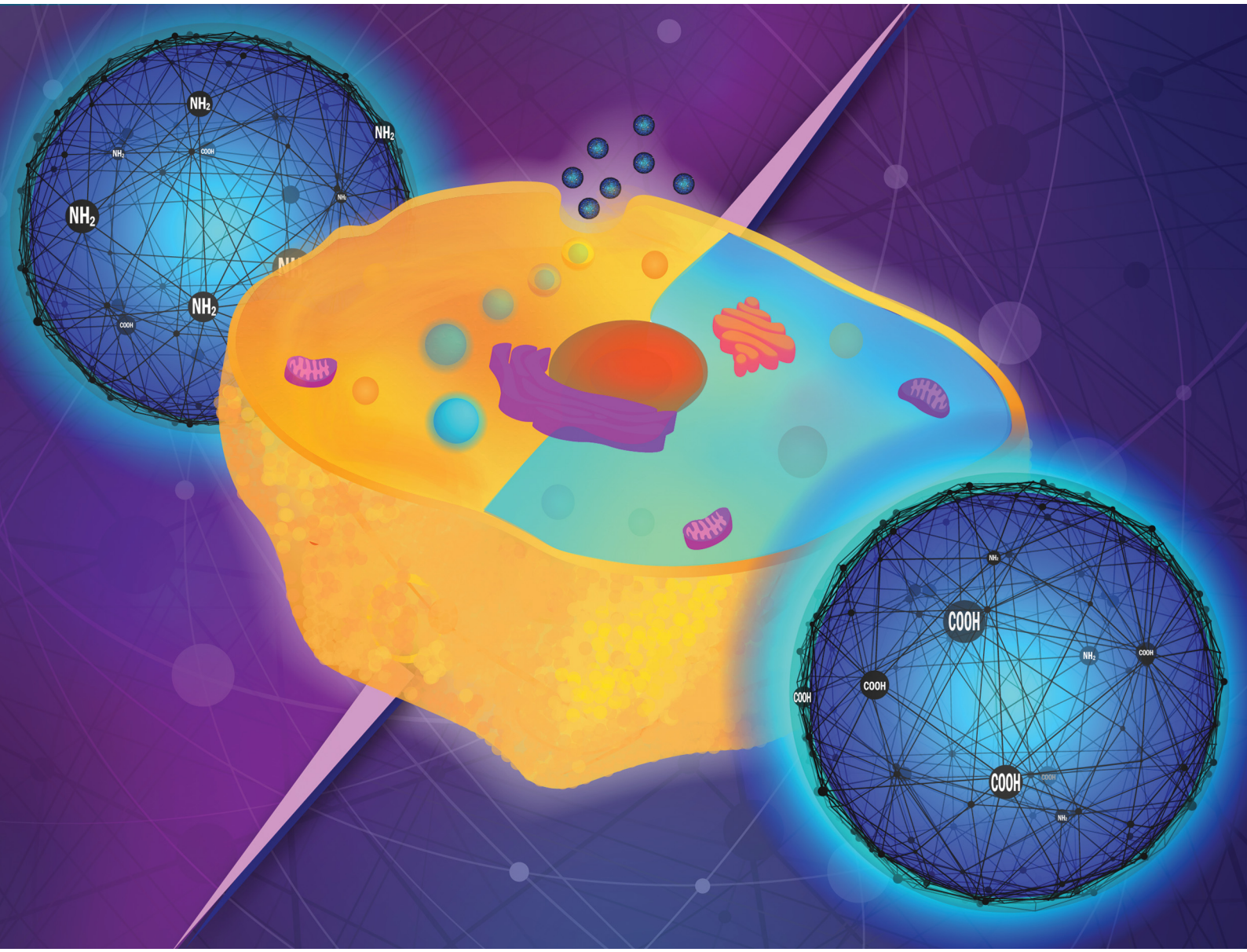

ISSN 2633-5409

ROYAL SOCIETY OF CHEMISTRY

PAPER

Alisa Piekny, Rafik Naccache *et al.*
Shining a light on cells: amine-passivated fluorescent carbon dots as bioimaging nanoprobes

Materials Advances

ROYAL SOCIETY OF CHEMISTRY

PAPER

View Article Online
View Journal | View Issue

Cite this: *Mater. Adv.*, 2024, 5, 3662

Shining a light on cells: amine-passivated fluorescent carbon dots as bioimaging nanoprobes†

Adryanne Clermont-Paquette,[abc] Kevin Larocque,[c] Alisa Piekny*[c] and Rafik Naccache *[ab]

Carbon dots (CDs) have garnered significant interest due to their optical properties and potential applications in cell and tissue imaging. While the physicochemical properties of CDs are predicted to impact their uptake and localization in cells, few studies have directly compared CDs derived from related chemical species, yet such studies are key to revealing structure–function relationships. Herein, CDs synthesized from citric acid and five different amine passivating agents were characterized to determine how an increase in amine composition affects their physicochemical properties, uptake, and localization in HeLa (human cervical carcinoma) and HFF-1 (human foreskin fibroblast) cells. We found that all CDs have similar functional groups and fluorescence properties with monodisperse sizes ranging from 1.3 to 2.7 nm. Their surface charge increases with amine passivation, which correlated with an increase in CD uptake in both cell lines. All CDs exhibited low cytotoxicity and localized to the lysosomes in both HeLa and HFF-1 cells. However, CDs prepared using pentaethylenehexamine (PH6-CDs) were more enriched in the lysosomes compared to the other CDs, while CDs prepared using diethyltriamine (DT3-CDs) were more cytosolic. Indeed, DT3-CDs have amphiphilic properties which may permit passive entry, while hydrophilic PH6-CDs likely rely more heavily on endocytic uptake. Our findings reveal how surface chemistry directs subcellular localization, which can be used to design imaging probes that target specific cellular compartments.

Received 13th September 2023,
Accepted 12th December 2023

DOI: 10.1039/d3ma00702b

rsc.li/materials-advances

Introduction

Carbon-based nanoparticles have emerged as a compelling class of materials with immense promise for a diverse array of biological applications.[1–3] Within this realm, carbon nanotubes, graphene, and carbon dots have characteristics that are ideal for biological applications.[4,5] Carbon nanotubes (CNTs) have cylindrical structures and have garnered attention for their outstanding electrical conductivity and mechanical robustness. Their properties are also useful for biological applications such as cellular imaging, drug delivery, and tissue engineering.[6] Similarly, graphene, composed of a single layer of carbon atoms arranged in a two-dimensional honeycomb lattice, boasts extraordinary mechanical strength, electrical conductivity, and a high surface area, making it useful for biosensing, biomolecule immobilization, and biocompatible interfaces.[7,8] Our research is focused on carbon dots; a class of carbon-based nanoparticles that have captured the scientific community's attention since their discovery by Xu *et al.* in 2004.[9]

Carbon dots (CDs) are small quasi-spherical carbon-based nanoparticles, typically measuring around ~10 nm, and are predominantly composed of carbon, hydrogen, oxygen, and nitrogen.[10–12] The appeal of CDs lies in their facile and cost-effective synthesis, which can be accomplished using a variety of organic materials such as orange juice, candle soot, leaves, monosaccharides, citric acid, and amino acids.[13] CDs have tunable fluorescence across the ultraviolet (UV) and visible regions of the spectrum. This fluorescence is characterized by high quantum yields ranging from 10% to 80%, and although the exact mechanism behind CD fluorescence is not fully understood, factors such as the quantum confinement effect, core, and surface states are believed to contribute.[14–16]

Importantly, CDs are photostable with resistance to photobleaching and blinking, and can be designed to have

[a] *Department of Chemistry and Biochemistry and Center for NanoScience Research, Concordia University, Montreal, QC, H4B 1R6, Canada. E-mail: rafik.naccache@concordia.ca*
[b] *Quebec Centre for Advanced Materials, Department of Chemistry and Biochemistry, Concordia University, Montreal, QC, H4B 1R6, Canada*
[c] *Department of Biology and the Centre for Microscopy and Cellular Imaging, Concordia University, Montreal, QC, H4B 1R6, Canada. E-mail: alisa.piekny@concordia.ca*

† Electronic supplementary information (ESI) available. See DOI: https://doi.org/10.1039/d3ma00702b

temperature or pH-sensitivity making them ideal for bioimaging applications and as sensors to monitor environmental and biological changes.[17–19] CDs also have low cytotoxicity and are predicted to be biocompatible, although more studies are needed to explore their compatibility with a broad range of tissues and organisms.[20–22]

The physicochemical properties of CDs can profoundly influence cellular uptake, localization, and fluorescence; however, how different properties affect their uptake in different cell types is not well understood. Most biological studies of CDs focus primarily on toxicity assessments, typically limited to a single cell type, and may not incorporate experiments to accurately assess mechanisms controlling their uptake and localization. Given that CDs are promising candidates for bioimaging applications, it is crucial to gain knowledge of their behaviour in a diverse range of cell types and tissues.[23] The uptake and subcellular localization of CDs are governed by multiple factors, including their size, shape, surface charge, and functionality.[24] CDs have been shown to enter cells through multiple mechanisms, including passive diffusion and endocytosis.[25] Unlike larger nanoparticles that may rely on micropinocytosis or receptor-mediated uptake, CDs can readily enter cells *via* non-receptor mediated endocytosis or possibly by passive diffusion owing to their small size and favourable physicochemical properties.[25] Fluorescent CDs synthesized from 2,5-deoxyfructosazine and averaging 2.4 nm in size were shown to predominantly enter HeLa (human cervical carcinoma) and HDF (human dermal fibroblast) cells *via* passive entry. These CDs were shown to cause selective LED-photothermal ablation of HeLa cancer cells in comparison to the HDF cells, showing promising theranostic applications.[26] Moreover, the fluorescence properties of CDs can change with different types of functionalization and passivation. Lu *et al.* (2015) found that CDs doped with ethanolamine were ideal for sensing and bioimaging applications in HeLa cells when compared to CDs doped with ethane sulfonic acid.[27] Their findings emphasize the significance of selecting appropriate precursors when designing CDs for biological applications. Different types of passivation can also affect the physicochemical properties of CDs, including quantum yield. Sachdev *et al.* (2014) synthesized CDs passivated with polyethylene glycol (PEG) and polyethyleneimine (PEI) and analyzed their physicochemical and bioimaging properties, as well as their uptake in BHK-21 (baby hamster kidney) and A549 (lung carcinoma) cells. Overall, they demonstrated that PEI-CDs were more promising for bioimaging applications due to their increased cellular uptake and fluorescent intensity in both cell types. In addition, the PEI-CDs were less cytotoxic at higher concentrations in both cell lines compared to PEG-CDs.[28] However, while numerous studies have explored the physicochemical properties and cytotoxicity of different CDs, our knowledge of how specific types of functionalization affects their mechanisms of uptake and localization in different cell types remains limited.

In recent years, efforts have been made to design CDs that localize to specific organelles to study changes in their function in response to perturbations. For instance, Pan *et al.* (2015) synthesized CDs using formamide that emits across the entire visible spectra and studied their uptake in MCF7 (breast adenocarcinoma) cells. These CDs caused little cytotoxicity and fluorescence signal was observed throughout the cells, including in the nuclei.[29] However, CDs that enter cells *via* endocytosis will remain in vesicles that traffic to endosomes, and often terminate at the lysosomes. Many of these compartments are typically found near the nucleus, making them challenging to resolve spatially without proper markers and/or if the fluorescence images are saturated. It is noteworthy to mention that most CDs are <10 nm, yet the spatial resolution of light microscopy is 150–200 nm depending on the microscope. Studies have also shown that the optical properties of CDs could be affected by interactions within the subcellular environment. Macairan *et al.* (2019) designed dual emissive CDs that detect precise temperature changes in HeLa cells without causing cytotoxicity, providing insights into the potential use of CDs as nanothermometers for biological studies.[30] In other studies, the optical properties of CDs were shown to change in response to pH in lysosomes. This change in fluorescence signal has been harvested by many research groups to synthesize and design promising nanosensors.[31] For example, Macairan *et al.* (2020) generated dual emissive CDs to detect changes in lysosomal pH in glioblastoma cells (brain cancer) in response to drugs which are currently being evaluated as cancer therapies.[32] These studies highlight the versatility of CDs as probes for monitoring cellular processes and elucidating their dynamic behaviour in real-time. However, further investigations are needed to unravel the mechanisms underlying their uptake, localization, and interactions with different cell types. Understanding the factors that influence the behaviour of CDs within cells, such as size, shape, surface charge, and functionalization, will pave the way for the development of more efficient and targeted bioimaging tools.

In this study, we synthesized five different amine-passivated CDs and compared their uptake and localization in live HFF-1 and HeLa cells. By generating CDs that strategically vary in chemical composition, we determined how specific changes in surface passivation influence the optical properties and interaction of CDs with different cell types, which to our knowledge has not been done before. Amine passivation was previously shown to enhance photostability and quantum yield, increase cellular uptake and reduce cytotoxicity.[30] Here, we found that increasing the extent of amine passivation had little effect on the optical properties, size or shape and the surface functionalization of CDs. However, we observed differences in surface charge that correlated with their cellular uptake and subcellular localization in both HFF-1 and HeLa cells. In particular, CDs with the greatest amine passivation and highest surface positive charge had the greatest uptake and localized more strongly to lysosomes in both cell types albeit to varying extents, while those with more amphiphilic properties were more cytosolic. These differences could be harnessed for specific bioimaging applications and/or drug delivery.

Experimental

Chemicals and reagents

Citric acid, ethylene-diamine (ED2), diethyltriamine (DT3), tetraethylenetriamine (TT4), tetraethylenepentamine (TP5), pentaethylenehexamine (PH6), acetone and ethanol were purchased from Sigma Aldrich. Milli-Q water was produced in-house. Phosphate buffer solution (PBS, pH 7.4, 1X) and Dulbecco's Modified Eagle Medium (DMEM) were purchased from Wisent. HyClone™ Cosmic Calf Serum (CCS) and HyClone™ Fetal Bovine Serum (FBS) were purchased from Cytiva, while LysoTracker™ Red DND-99 was purchased from Thermo Scientific. The WST-8 Cell Proliferation Assay Kit was purchased from Cayman Chemical. All reagents were of analytical grade and were used as is, without the need for further purification.

Synthesis of carbon dots

All CDs were synthesized using a CEM Discover SP microwave reactor. For the synthesis of all CDs, 0.384 g (500 mM) of citric acid was added to 4 mL of distilled water and 375 mM of the amine passivating agent in a microwave reaction tube. The amine passivating agents used were ethylene-diamine (ED2), diethyltriamine (DT3), tetraethylenetriamine (TT4), tetraethylenepentamine (TP5), and pentaethylenehexamine (PH6). The solutions were sonicated for 15 minutes, or until a homogenous solution was observed. The mixed solutions were then heated to 210 °C for 10 minutes. After the reactions were complete, they were dialyzed in Milli-Q water using a cellulose dialysis membrane (molecular weight cut-off = 3.5–5.0 kDa) to remove excess material. The samples were dialyzed for 5 days, and the water was changed twice per day. A decrease in colour correlated with the removal of unwanted products. The samples were then purified by washing twice with acetone and twice with ethanol. After each wash, the precipitate was collected by centrifugation at 10 000 rpm × for 10 minutes, and the supernatant was discarded. The remaining precipitate was left to dry for 12 to 24 hours in an oven at 80 °C, then crushed into a fine powder and resuspend in ultrapure water. Finally, for biological purposes and to prevent contamination, the resuspended materials were filtered through a 0.22 μm nylon filter.

Fluorescence spectroscopy

The fluorescence spectra of the CDs were measured using a Cary Ellipse Fluorescence Spectrophotometer (Agilent Technologies) in a 1 cm quartz cuvette. Prior to analysis, the concentration was adjusted to an absorbance value of 0.1 a.u. to avoid potential inner filter effects. All fluorescence data was collected by setting λ_{ex} at 350 nm over a range of 200 to 800 nm (at 1 nm intervals). The excitation and emission slits were set to a width of 5 nm with a PMT voltage at 600 V and a scan rate of 600 nm min^{-1}. All data was processed using Cary Eclipse software. Background corrections were made to account for the solvent (Milli-Q water).

UV-vis absorbance spectroscopy

Absorbance was measured using a Cary 5000 series UV-Vis-NIR Spectrophotometer (Agilent Technologies). The UV-visible absorption spectra were collected over a range of 200–800 nm using a 1 cm quartz cuvette. A resolution of 1 nm and a bandwidth of 2 nm with a scan speed of 600 nm s^{-1} and wavelength at 350 nm was used for analysis. Data was processed using Cary Eclipse software, and the background was corrected for solvent (Milli-Q water).

Fourier transform infrared spectroscopy

FTIR spectra were collected using a Thermo Scientific Nicolet iS5 equipped with an iD5 ATR accessory. Approximatively 10 μg of each CD was used for analysis. The spectra were collected with 64 scans at a resolution of 0.4 cm^{-1}, gain of 1, optical velocity of 0.4747, and an aperture setting of 100. Data was processed using Omnic 9 software.

Transmission electron microscopy

TEM grids (3 mm, 200 mesh Lacey/carbon-coated copper grid) were prepared by pipetting a 2 μg mL^{-1} dispersion of each CD onto the grid followed by evaporation of the isopropanol solvent. TEM images were collected using a Talos microscope operating at 120 kV. The images were processed, and the carbon dot sizes were measured using Fiji imaging software. The TEM tiff files for each CD were transferred to Fiji imaging. Using the straight-line tool, the diameter (in nanometer) of a minimum of 50 individual nanoparticles was measured, and values were graphed in a histogram to reveal their Gaussian distribution.

Quantum yield

Quantum yield values were acquired using a PTI QuantaMaster 8075 spectrofluorometer (Horiba) equipped with a 75 W Xenon lamp and a Czerny–Turner monochromator and an integrating sphere (K-Sphere Petit, Horiba). The quantum yield was determined by the absolute method in which the number of absorbed photons of a sample and the number of consequently emitted photons were measured. All quantum yield measurements were done in Milli-Q water in a 1 cm quartz cuvette, with the excitation and emission slits set to a width of 5 nm, and excitation at 350 nm. The spectra from 3000–800 nm were collected. The quantum yields were collected from spectra between 300–550 nm. Scans were done in triplicate with a dwell time of 0.25 seconds, and data was processed using FelixGX software.

$$\text{QY } \% = \frac{\text{photons emitted}}{\text{photons absorbed}} \times 100\%$$

Zeta-potential

Zeta-potential measurements were acquired using a Malvern Zetasizer Nano ZSP with colloidal dispersion of each amine passivated CDs (Ed2-, DT3-, TT4-, TP5- and PH6-CDs) at a final concentration of 10 μg mL^{-1} in Milli-Q water. Zeta-potential values are reported as the average of 3 independent batches of each CD.

Photobleaching

Aqueous dispersions of ED2-, DT3-, TT4-, TP5-, and PH6-passivated CDs were prepared at final concentration of

10 μg mL^{-1} in 40 mL volumes. Each dispersion was placed under a 15 W UV lamp for 0, 0.33, 0.5, 0.66, 1, 2, 3, 6, and 12 hours using a UVP Chromato-VUE® C-70G viewing cabinet. At every timepoint, an aliquot was removed to record its respective fluorescence intensity. The remaining percent fluorescence was calculated with the following equation.

$$\text{Remaining Fluorescent \%} = \frac{\text{Fluorescent intensity at } x \text{ point time}(\lambda_{ex} = 350\ \text{nm})}{\text{Fluorescent intensity at time point 0}(\lambda_{ex} = 350\ \text{nm})}$$

Log *P* partition coefficient for DT3-CDs and PH6-CDs

We prepared separate solutions of water and octanol with a known concentration of DT3-CDs and PH6-CDs. A series of standard solutions of the test compound in both water and octanol was prepared and their respective absorbance was measured. We then plotted the absorbance values against the corresponding concentrations to create calibration curves for water and octanol. The partition coefficient was determined by taking 10 mL of water and 10 mL of octanol and adding 0.001 g of DT3-CDs and or PH6-CDs. The solution was shaken vigorously for a sufficient time to allow equilibrium to be reached between the water and octanol phases, then the solution was given time to settle until the phases had visually separated. A sample of each phase was collected, and the absorbance was measured using the UV-Visible spectrophotometer at the same wavelengths used for calibration.

The log *P* partition coefficient was then calculated using the following equation:

$$\text{Log}\,P = \log 10\left(\frac{[\text{octanol}]}{[\text{water}]}\right)$$

where, [octanol] and [water] are the concentrations of the compound in octanol and water, respectively.

Cell culture

HFF-1 (human foreskin fibroblast) cells were cultured in DMEM (Wisent) supplemented with 10% (v/v) FBS (Cytiva) and 2 nM L-Glutamine (Wisent). HeLa (human cervical adenocarcinoma) cells were cultured in DMEM (Wisent) supplemented with 10% (v/v) CCS (Cytiva) and 2 nM L-Glutamine (Wisent). Cells were maintained in a humidified incubator set to 37 °C with 5% CO_2 and passaged at 75–100% confluency or as needed for the analysis of CDs in cells.

To measure CD uptake, cells were plated in 12-well glass bottom dishes (CellVis) at a confluency of 30–40% (HeLa) or 50–60% (HFF-1). Cells were treated with 100 μL of each CD adjusted to the same optical density over 24 hours to assess their fluorescence intensity in cells (ED2, DT3, PH6 at 1000 μg mL^{-1}, TT4 at 750 μg mL^{-1} and TP5 at 600 μg mL^{-1}). Prior to imaging, the cells were washed with 1X PBS (phosphate-buffered saline) and replaced with fresh, pre-warmed media.

To monitor CD localization, cells were plated on individual 35 mm glass bottom dish (CellVis) at a confluency of 30–40% (HeLa) or 50–60% (HFF-1) and were treated with 1000 μg mL^{-1} of CDs for 24 hours. To image the lysosomes, LysoTracker™ DND-99 was added to treated cells at a final concentration of 75 nM and left in the incubator for 45 minutes before imaging. Prior to imaging, cells were washed with 1 X PBS (phosphate-buffered saline) and replaced with fresh, pre-warmed media.

Cytotoxicity

HFF-1 and HeLa cells were plated in 96-well dishes at 4000–5000 cells per well and left to adhere for 24 hours. Then, cells were treated with increasing concentrations of each CDs (0 to 10 000 μg mL^{-1}) for three generation times (72 and 108 hours for HeLa and HFF-1 cells, respectively). Cytotoxicity was assessed using the WST-8 cell proliferation assay (Cayman Chemical) as per manufacturer's instructions. For each well, 10 μL of reagent was added for 4 hours, then the optical density (OD) values were obtained using the TECAN 200 PRO plate reader at a wavelength of 490 nm. Cell viability was measured as a ratio of the signal of treated cells *vs.* control (untreated cells):

$$\%\ \text{cell viability} = \frac{\text{OD}(490\ \text{nm})_{\text{sample}}}{\text{OD}(490\ \text{nm})_{\text{control}}} \times 100\%$$

The experiments were repeated in triplicate and the means were plotted with standard deviation using GraphPad Prism software. The IC_{50} was obtained by measuring the concentration at which half the population (50%) remained alive with CD treatment. HeLa and HFF-1 cells were imaged using a Nikon brightfield microscope to ensure that they were plated with the appropriate confluency, and to ensure that changes in density were not caused by contamination or other unrelated issues.

Microscopy

Cells were imaged using the Nikon-TiE inverted epifluorescence microscope with a Lambda XL Xenon light source using a 60× Plan Apo objective lens (NA1.4) or a 100× S Fluor objective lens (NA 1.3), a Piezo Z stage (ASI), a Photometrics Evolve 512 EMCCD camera and Elements 4.0 acquisition software (Nikon). A Sutter Lambda XL Xenon-arc lamp filtered by a 380/12 nm bandpass filter was used to excite carbon dots, and the emitted light was collected using a 400–600 nm bandpass filter (Chroma CT500/200bp). To capture red fluorescence from the LysoTracker RED, a 577/25 nm excitation filter and 585 nm longpass emission filter were used. The images were exported as TIFFs and used for analysis.

Statistical analysis

The TIFFs of HeLa and HFF-1 cells treated with the different CDs were used to assess the cellular uptake of CDs. The mean intensity was measured for each CD in each cell type (ED2-CDs: $n_{HeLa} = 29$; $n_{HFF\text{-}1} = 27$/DT3-CDs: $n_{HeLa} = 29$; $n_{HFF\text{-}1} = 27$/TT4-CDs: $n_{HeLa} = 32$; $n_{HFF\text{-}1} = 25$/TP5-CDs: $n_{HeLa} = 28$; $n_{HFF\text{-}1} = 25$/PH6-CDs: $n_{HeLa} = 27$; $n_{HFF\text{-}1} = 31$), and the background was subtracted using a thresholding tool. The mean intensity values were then plotted on a whisker box plot and a one-way ANOVA was

performed along with a post-hoc paired *t*-test to assess for statistical significance.

The extent of co-localization of the different CDs in HeLa and HFF-1 cells with the lysosome marker lysotracker was measured from the TIFFs. To do this, the TIFFs were first deconvolved using AutoQuant X, then the Biop Jacop plugin in Fiji was used to calculate the Pearson's correlation coefficient between the two channels (ED2-CDs: n_{HeLa} = 11; $n_{HFF\text{-}1}$ = 19/DT3-CDs: n_{HeLa} = 11; $n_{HFF\text{-}1}$ = 19/TT4-CDs: n_{HeLa} = 11; $n_{HFF\text{-}1}$ = 23/TP5-CDs: n_{HeLa} = 11; $n_{HFF\text{-}1}$ = 23/PH6-CDs: n_{HeLa} = 21; $n_{HFF\text{-}1}$ = 40). The values (% correlation) were then plotted on a whisker box plot and a one-way ANOVA was performed along with a post-hoc paired *t*-test to test for statistical significance.

Lastly, the TIFFs were also used to measure the proportion of CDs in the cytosol of HeLa and HFF-1 cells. The images were corrected for background, then the mean intensity was determined from the average of three regions of interest in the cytosol. Each measurement was performed in triplicates (ED2-CDs: n_{HeLa} = 14; $n_{HFF\text{-}1}$ = 23/DT3-CDs: n_{HeLa} = 12; $n_{HFF\text{-}1}$ = 23/TT4-CDs: n_{HeLa} = 12; $n_{HFF\text{-}1}$ = 24/TP5-CDs: n_{HeLa} = 15; $n_{HFF\text{-}1}$ = 23/PH6-CDs: n_{HeLa} = 13; $n_{HFF\text{-}1}$ = 24). The mean intensity values divided by a factor of 10 and then plotted on a whisker box plot and a one-way ANOVA was performed along with a post-hoc paired *t*-test to determine statistical significance.

Results

Optical properties of amine-passivated CDs

Five different amine-passivated CDs were synthesized, and their optical properties were compared, which could be influenced by factors such as the quantum confinement effect, core, and surface states. The CDs were synthesized using a microwave-mediated reaction with 500 mM of citric acid and 375 mM of passivating agents with increasing numbers of amines; ethylenediamine (ED2), diethyltriamine (DT3), tetraethylenetriamine (TT4), tetraethylenepentamine (TP5) and pentaethylenehexamine (PH6). The functionalized CDs were first characterized using absorption and fluorescence spectroscopy. The absorption spectra of the CDs showed two main absorption bands centered at 240 and 350 nm, which reflect the π → π* transition of the aromatic sp^2 domains, and the n → π* transition of the C═O bond or amine functional groups, respectively (Fig. 1A). The CDs also displayed a single fluorescence centered at 480 nm following excitation using a λ_{max} = 350 nm (Fig. 1A and Fig. S1 (ESI†) for the excitation spectra). The CDs also displayed a single fluorescence centered at 480 nm following excitation using a λ_{max} = 350 nm (Fig. 1A). The fluorescence quantum yield of the different CDs was also measured using an integrating sphere and determined to be 15%, 25%, 10%, 22% and 20% for ED2, DT3, TT4, TP5 and PH6-passivated CDs, respectively. Notably, there were no significant differences or correlation in quantum yield that can be ascribed to the amine content of the precursors. All CDs show a strong emission in the blue spectra which could come from interactions between the core and the surface state due to extensive amine passivation (Fig. 1B). It is possible that certain nitrogen sources, such as ED2 and TT4, may not be as effective in enhancing radiative recombination or mitigating surface defects in these CDs, explaining their lower quantum yield, compared to the other.

Physicochemical properties of amine-passivated CDs

Next, we evaluated the physicochemical properties of the different CDs. Specifically, we investigated their surface composition, charge, size and shape. As shown in Fig. 2A, Fourier transform infrared spectroscopy (FT-IR) was utilized to assess the chemical groups on the surface of the different CDs, and the results revealed that all CDs have similar spectra with a

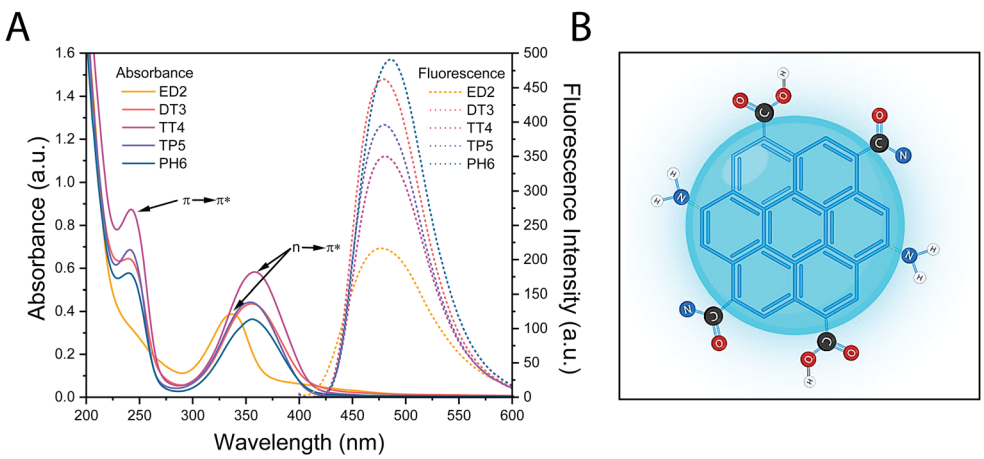

Fig. 1 Optical properties of amine-passivated CDs. (A) Room temperature absorbance and fluorescence spectra of each CD in an aqueous solution. The UV-Vis absorption spectrum of each CD (line curve) reveals two absorption bands centered at 240 nm and 335–355 nm, which reflect the π → π* and n → π* transition, respectively. Following maximum excitation at 350 nm one emission maxima is measured at 480 nm (dotted curve). (B) Graphic representation of CD fluorescence *via* molecular/core state mechanism. The brighter blue ring represents the surface to which different functional groups are directly bound to the core of the CD. In this image the strong blue emission comes from both the core and the surface as a result of the amine passivation that enhance the core state and decreases the surface state.

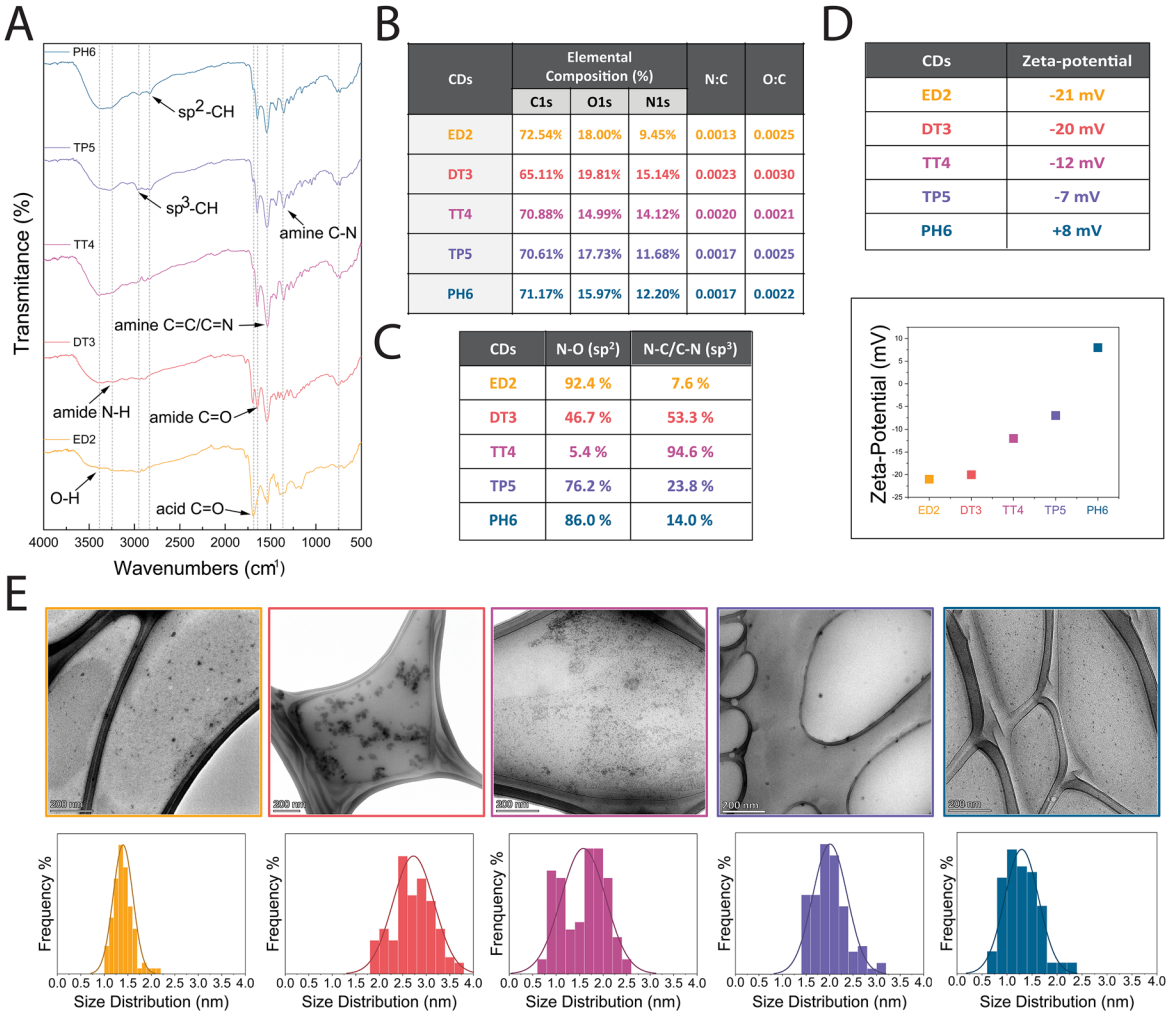

CDs	Elemental Composition (%)			N:C	O:C
	C1s	O1s	N1s		
ED2	72.54%	18.00%	9.45%	0.0013	0.0025
DT3	65.11%	19.81%	15.14%	0.0023	0.0030
TT4	70.88%	14.99%	14.12%	0.0020	0.0021
TP5	70.61%	17.73%	11.68%	0.0017	0.0025
PH6	71.17%	15.97%	12.20%	0.0017	0.0022

CDs	N-O (sp^2)	N-C/C-N (sp^3)
ED2	92.4 %	7.6 %
DT3	46.7 %	53.3 %
TT4	5.4 %	94.6 %
TP5	76.2 %	23.8 %
PH6	86.0 %	14.0 %

CDs	Zeta-potential
ED2	-21 mV
DT3	-20 mV
TT4	-12 mV
TP5	-7 mV
PH6	+8 mV

Fig. 2 Physico and chemical properties of amine-passivated CDs. (A) A graph shows the stacked FT-IR spectra for each of the amine-passivated CDs. The broad carbonyl signal from 1614 to 1753 cm^{-1} indicates carboxylic acid (C═O), and sp^3 and sp^2 C–H peaks are at 2964 cm^{-1} and 2830 cm^{-1} respectively. Lastly, amide C═O, C═C/C═N, and N–H/C–N peaks appears at 1646 cm^{-1}, 1536 cm^{-1} and 1354 cm^{-1}. (B) A table shows the elemental composition determined by XPS for the N : C and O : C ratios. (C) A table shows the N–O (sp^2) *vs.* N–C/C–N (sp^3) composition for each CD. (D) A table (top) and graph (bottom) show the zeta-potential for the different CDs, as an indication of surface charge. (E) CDs are quasi-spherical and are close to 2 nm in size. TEM images show aqueous dispersions of the different amine-passivated CDs as indicated. The CDs are quasi-spherical with sizes of 1.4 ± 0.2 nm, 2.7 ± 0.5 nm, 1.6 ± 0.5 nm, 2.0 ± 0.4 nm, and 1.3 ± 0.3 nm for the ED2-, DT3-, TT4-, TP5- and PH6-passivated CDs, respectively. The size measurements for each of the CDs were spread over a Gaussian distribution ranging from 0 to 4.5 nm.

broad carbonyl signal from 1614 to 1753 cm^{-1} associated with the presence of carboxylic acid (C═O). Additionally, sp^3 C–H peaks were detected at 2964 cm^{-1} and sp^2 C–H peaks in the 2830 cm^{-1} region, while amide C═O, C═C/C═N, and amine N–H/C–N peaks appeared at 1646 cm^{-1}, 1536 cm^{-1}, and 1354 cm^{-1}, respectively. Although the spectra were comparable, there was a noticeable decrease in the carboxylic acid signal with increased passivation, and a corresponding increase in the C═C/C═N and N–H/C–N peaks.

The elemental composition of the different CDs was determined by X-ray photoelectron spectroscopy (XPS) analysis, which measures the binding energies for C1s, N1s, and O1s at 280, 400, and 530 eV, respectively. We found that each CD was mainly composed of carbon (~70.17%), oxygen (~17.30%) and nitrogen (~12.52%) (Fig. 2B). As shown in Fig. S2 (ESI†), deconvolution of the C1s peak revealed three main peaks at 285, 286, and 288 eV, attributed to C–C, C–O, and carboxylic C═O groups, respectively. The N1s peak showed two main peaks at 399 and 400 eV caused by amine N–C and amide N–O, respectively. Lastly, the O1s peak had two main peaks at 531 and 532 eV due to carboxyl C═O and carbonyl C–O groups. These XPS results are supported by the FTIR results.

The XPS elemental composition analysis also revealed higher nitrogen content in DT3-CDs (15.14%) in comparison to TT4-, TP5-, and PH6-CDs (14.12%, 11.68% and 12.20%) despite the latter being passivated with reagents that have more amine groups (Fig. 2B). To determine why this unexpected decrease occurred, we performed a more detailed XPS analysis to measure the N–O sp^2 amide and N–C/C–N sp^3 amine content. As shown in the table presented in Fig. 2C, the surface

of DT3- and TT4-CDs contained more amine groups (53.3% and 94.6%) while ED2-CDs, TP5- and PH6-CDs possessed more amides (92.4%, 76.2% and 86.0%). This phenomenon could be explained by the molecular structure of the precursors used to prepare the CDs, and the relative ratio of carboxylate groups and amines that could cause amidation and/or the formation of heteroaromatic rings contributing to the core *vs.* the surface chemical makeup. The surface charge of the different CDs was evaluated to predict their cellular uptake, as previous studies suggested that uptake occurred more favourably with nanoparticles that were more positively charged.[33,34] To evaluate their surface charge, the different CDs were dispersed in an aqueous solution to a final concentration of 10 μg mL^{-1} and their zeta potential was measured. The results showed that the surface charges of ED2-, DT3-, TT4-, TP5-, and PH6-CDs were −21 mV, −20 mV, −12 mV, −7 mV, and +8 mV, respectively (Fig. 2D). This near linear increase in positive surface charge is proportional to the increase in amine content in the passivating agents.

The shape, size and dispersibility of the different CDs were analyzed, as these parameters can also affect cellular uptake. The TEM images shown in Fig. 2E revealed that the different CDs are quasi-spherical with sizes of 1.4 ± 0.2 nm, 2.7 ± 0.5 nm, 1.6 ± 0.5 nm, 2.0 ± 0.4 nm, and 1.3 ± 0.3 nm for ED2-, DT3-, TT4-, TP5-, and PH6-CDs, respectively. The size measurements of each CD showed a Gaussian distribution ranging from 0.6 to 3.8 nm. We also measured their polydispersity indexes (PDIs), which ranged from 0.02 to 0.07. These low PDI values suggest that the CDs do no tend to aggregate, which is ideal for biological applications.[35] Overall, these data show that the different amine passivated CDs have similar morphology.

Finally, the different CDs were assessed for photostability, as their ability to retain fluorescence after long periods of light exposure would be advantageous. The CDs were resuspended in aqueous solution and exposed to 365 nm UV light for 0 to 12 hours. As shown in Fig. S3 (ESI†), the graph shows the % fluorescence remaining over time. There was little decrease in the fluorescence intensity of the TT4-, TP5- and PH6-CDs during the first 4 hours of exposure, which then dropped to ~35–40% after 12 hours. The intensity of ED2- and DT3-CDs dropped within 2–4 hours, and DT3-CDs had the least resistance with only 6.6% remaining fluorescence after 12 hours. As more exposure to light occurs, an irreversible loss of fluorescence typically occurs due to photobleaching and the degradation of chemical bonds. Although CDs typically possess surface defects and functional groups that can act as photoactive sites susceptible to photobleaching, their passivation with amine groups could potentially neutralize or block the reactive surface states, which increases their photostability.

Cytotoxicity of amine-passivated CDs

We tested the different amine-passivated CDs for cytotoxicity in both HFF-1 and HeLa cells. HFF-1 cells are foreskin fibroblast cells taken from a white, male patient, while HeLa cells are epithelial in origin and derived from a cervical adenocarcinoma taken from a black female patient, and differences in their tissue of origin, disease *vs.* healthy state and individual genetic backgrounds could influence their response to CDs. After exposing the cells to varying concentrations of CDs for three division cycles (108 hours for HFF-1 and 72 hours for HeLa), cell viability was measured using the WST-8 assay. As shown in Fig. S4 (ESI†), there was either no toxicity or it was very low for the different amine-passivated CDs in both cell types. Of the measurable IC_{50} values, ED2 was 10 000 μg mL^{-1} in HFF-1 and HeLa cells, while TP5 was 7500 μg mL^{-1} in HFF-1 cells. The other CDs showed no sign of toxicity in both HFF-1 and HeLa cells beyond 10 000 μg mL^{-1}. Thus, regardless of their extent of amine passivation, the CDs have little impact on the health of these diverse cell types.

Cellular uptake of amine-passivated CDs

Next, we compared the uptake of the different CDs in HFF-1 and HeLa cells. Since their size and surface composition are similar, charge is likely to be the main physicochemical property that could influence the uptake of amine passivated CDs, which range from being more negative (*e.g.*, ED2-CDs) to more positive (*e.g.*, PH6-CDs). To achieve this, HFF-1 and HeLa cells were treated for 24 hours with CDs adjusted to the same optical density to prevent concentration-dependent fluorescence, then imaged using widefield epifluorescence. As shown in Fig. 3A and B, there appeared to be a significant increase in the fluorescence intensity of CDs that positively correlated with the extent of amine passivation in both HFF-1 and HeLa cells. Indeed, measurements of the mean fluorescence intensity revealed a 5% and 20% increase in signal when HFF-1 and HeLa cells, respectively, were treated with PH6-CDs (Fig. 3C and D and Table S1, ESI†). This data suggests that CDs with positive surface charges may more readily be taken up by cells.

Subcellular localization of amine-passivated CDs

The different amine-passivated CDs were also assessed for their localization in HFF-1 and HeLa cells. Generally, CDs that enter cells *via* endocytosis will be trafficked to the lysosomes.[36–38] However, different physicochemical properties could influence the mechanism of CD uptake and cause differences in their subcellular localization, which could also vary with cell type. To determine how lysosome localization of the CDs differs in HFF-1 and HeLa cells, the cells were treated with LysoTracker dye, as well as 1000 μg mL^{-1} of each CD and imaged using epifluorescence microscopy. As shown in both Fig. 4A and 5A, there appeared to be an increase in the overlap (white signal) between the lysosome and CD signal as the extent of amine passivation increased (*e.g.*, ED2-CDs *vs.* PH6-CDs). The co-localization between the CDs and lysosome signal was then quantified using a plug-in for ImageJ to calculate the Pearson's correlation coefficient. As shown in the graphs in Fig. 4B and 5B, there was an increase in the localization of CDs with greater amine passivation in the lysosomes in both HFF-1 and HeLa cells. Specifically, we found that 12, 22, 36, 45, and 52% of ED2-, DT3-, TT4-, TP5-, and PH6-CDs, respectively, co-localized with the lysosomes in HFF-1 cells with significantly higher amounts of PH6-CDs compared to the other CDs (Fig. 4B and Table S2, ESI†). In HeLa cells, we found that 21, 21, 31, 49, and 80% of ED2-, DT3-, TT4-, TP5-, and PH6-CDs, respectively, co-localized

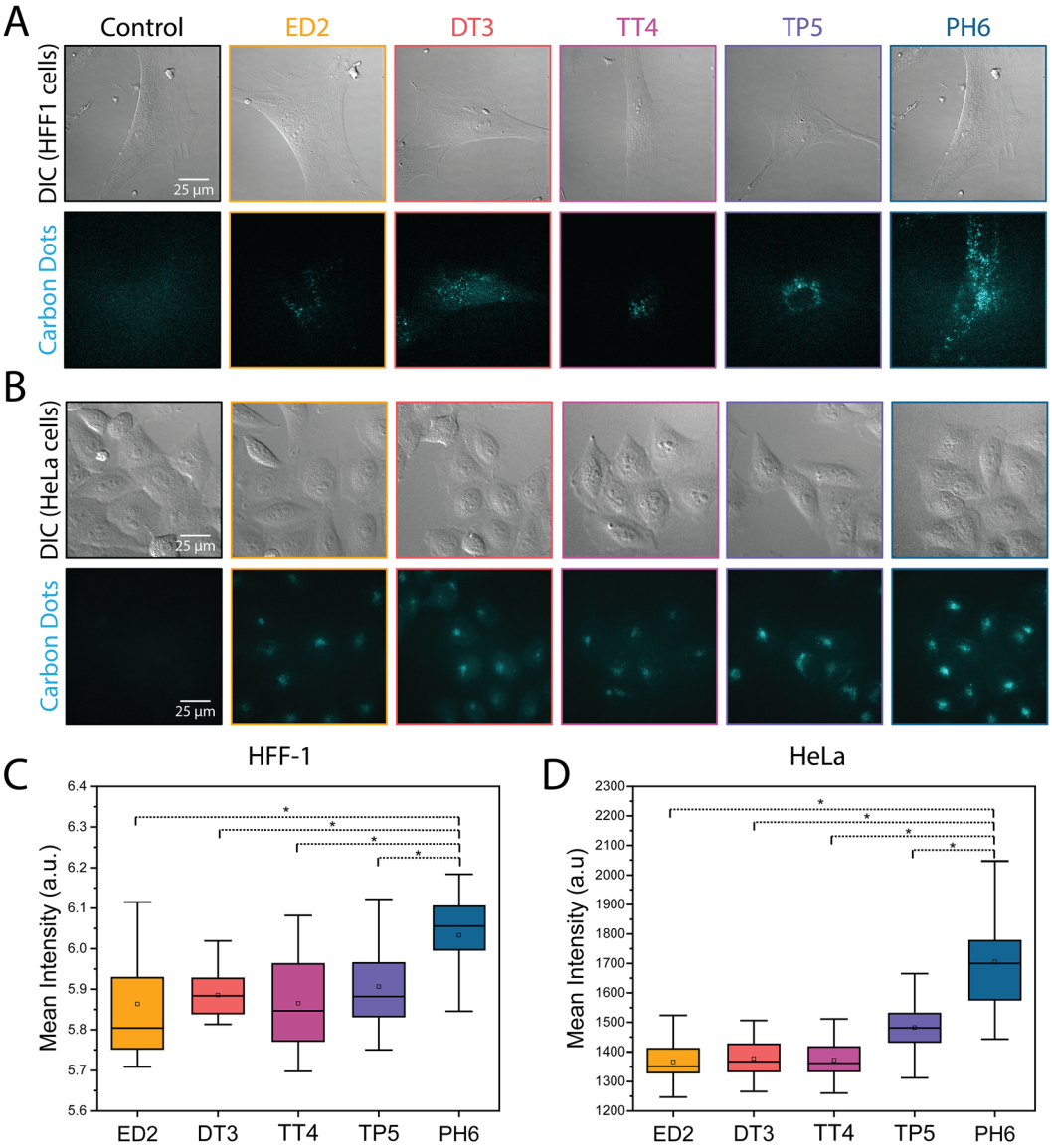

Fig. 3 Cellular uptake of CDs in HFF-1 and HeLa cells. (A) Brightfield (top) and fluorescence images (bottom) of HFF-1 cells 24 hours after treatment with the CDs (blue) as indicated. The scale bar is 25 µm. (B) Brightfield (top) and fluorescence images (bottom) of HeLa cells 24 hours after treatment with the CDs (blue) as indicated. The scale bar is 25 µm. (C) A box and whiskers plot show the mean intensity (a.u.) of the different CDs as indicated in HFF-1 cells. Bars indicate standard deviation. One-way ANOVA and paired *t*-tests to PH6 were done to show significance (*$p < 0.001$). (D) A box and whiskers plot shows the mean intensity (a.u.) the different CDs as indicated in HeLa cells. Bars indicate standard deviation. One-way ANOVA and paired *t*-tests to PH6 were done to show significance (*$p < 0.001$).

with lysosomes, with significantly more PH6-CDs compared to the other CDs (Fig. 5B and Table S3, ESI†). This data suggests that more PH6-CDs enter HFF-1 and HeLa cells *via* endocytosis compared to the other amine passivated CDs, which are more favourably endocytosed by HeLa *vs.* HFF-1 cells. Unexpectedly, we noticed that DT3-CDs appeared to be more enriched in the cytosol in both cell lines. To quantify this, we measured the mean signal intensity in the cytosol for the different CDs in both HFF-1 and HeLa cells. Indeed, DT3-CDs showed significant enrichment in the cytosol compared to the other CDs in both HFF-1 and HeLa cells (Fig. 4C, 5C and Table S2, S3, ESI†). This data suggests that these CDs could have entered cells passively or escaped from endosomes more easily than the other CDs.[39] To determine which explanation is more likely, we conducted a log*P* partitioning coefficient experiment for DT3-CDs and PH6-CDs and have found that the log*P* of DT3-CDs was −0.194 while it was −3.31 for PH6-CDs. This finding strongly shows that DT3-CDs have amphiphilic properties that could favour passive entry, while PH6-CDs are more hydrophilic and would rely on endocytic mechanisms for cellular uptake.[40]

Discussion

CDs have optical properties that could make them a promising tool for bioimaging applications in diagnostics and

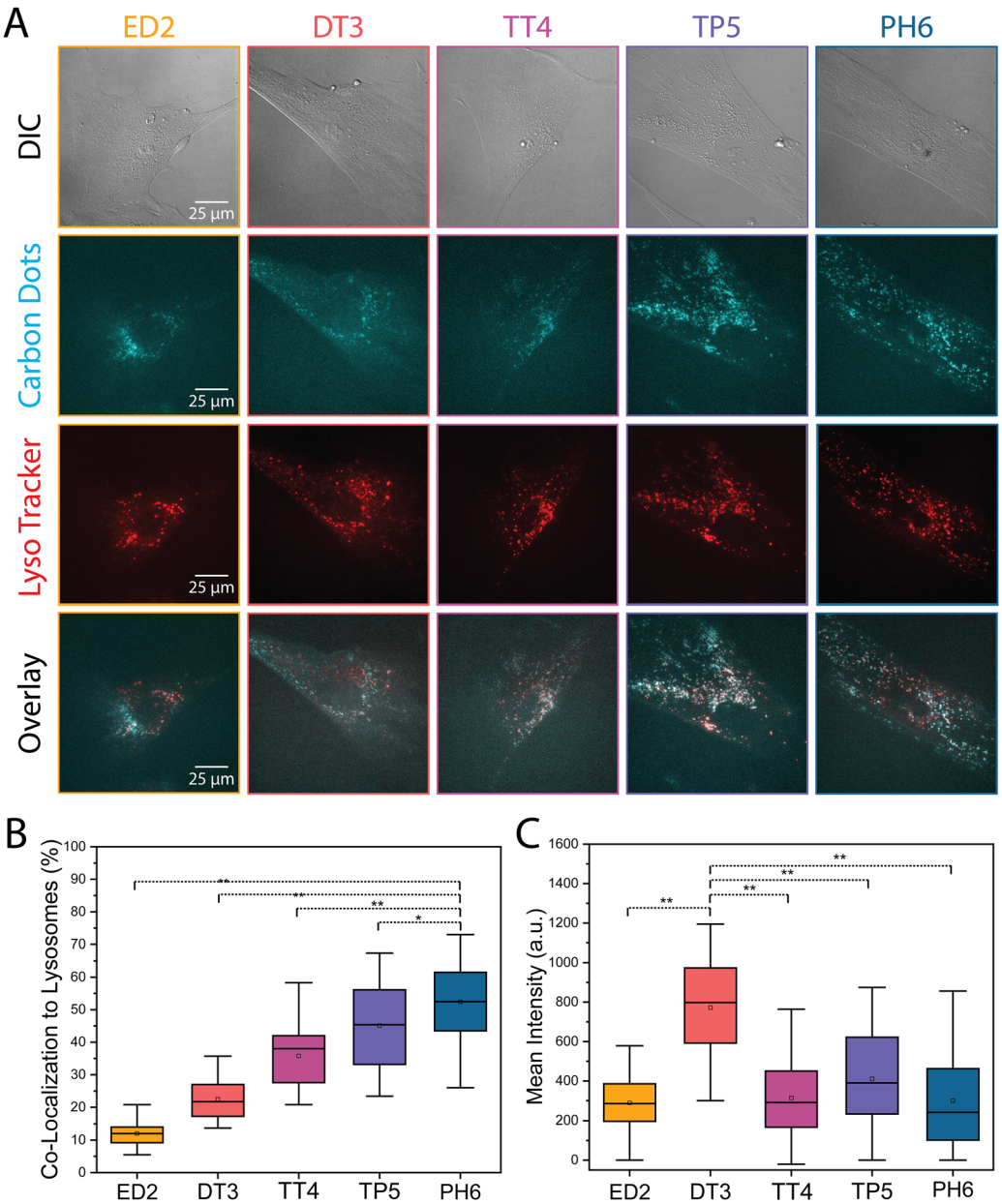

Fig. 4 CDs localize to the lysosomes and cytosol in HFF-1 cells. (A) Brightfield (top) and fluorescence images show live HFF-1 cells 24 hours after treatment with 1000 µg mL^{-1} of the CDs (blue) as indicated, co-stained for lysotracker (red). The scale bar is 25 µm. (B) A box and whiskers graph show the % co-localization of CDs as indicated with lysotracker using Pearson's correlation coefficient. Bars indicate standard deviation. One-way ANOVA and paired *t*-tests to PH6 were done to show significance (*$p < 0.05$; ** $p < 0.001$). (C) A box and whiskers graph shows the mean intensity (a.u.) of CDs in the cytosol. Bars indicate standard deviation. A one-way ANOVA and paired *t*-tests to DT3 were done to show significance (**$p < 0.001$).

therapeutics. However, few studies have examined CDs in biological contexts, and how specific changes in their physicochemical properties affect their uptake and localization in different cell types. This study compared CDs with increasing amine passivation and determined how this affects their physicochemical properties, uptake and localization in HFF-1 and HeLa cells. Although their optical properties are similar, PH6-CDs are more photostable and exhibited the highest fluorescent signal in both cell lines, indicating that a high quantum yield is not the only factor to consider for bioimaging applications. Further, although their size and shape are similar, there could be differences in the proportion of surface amides *vs.* amines, which could be explained by the molecular structure of the precursors and their incorporation into the carbon core *vs.* the surface of the dots. It is unclear whether these differences affect their ability to enter cells and/or their localization, since ED2-CDs and PH6-CDs had similar proportions of amides: amines, yet much fewer ED2-CDs were taken up by cells compared to PH6-CDs, which showed the strongest fluorescent signal. Importantly, we found that the extent of CD

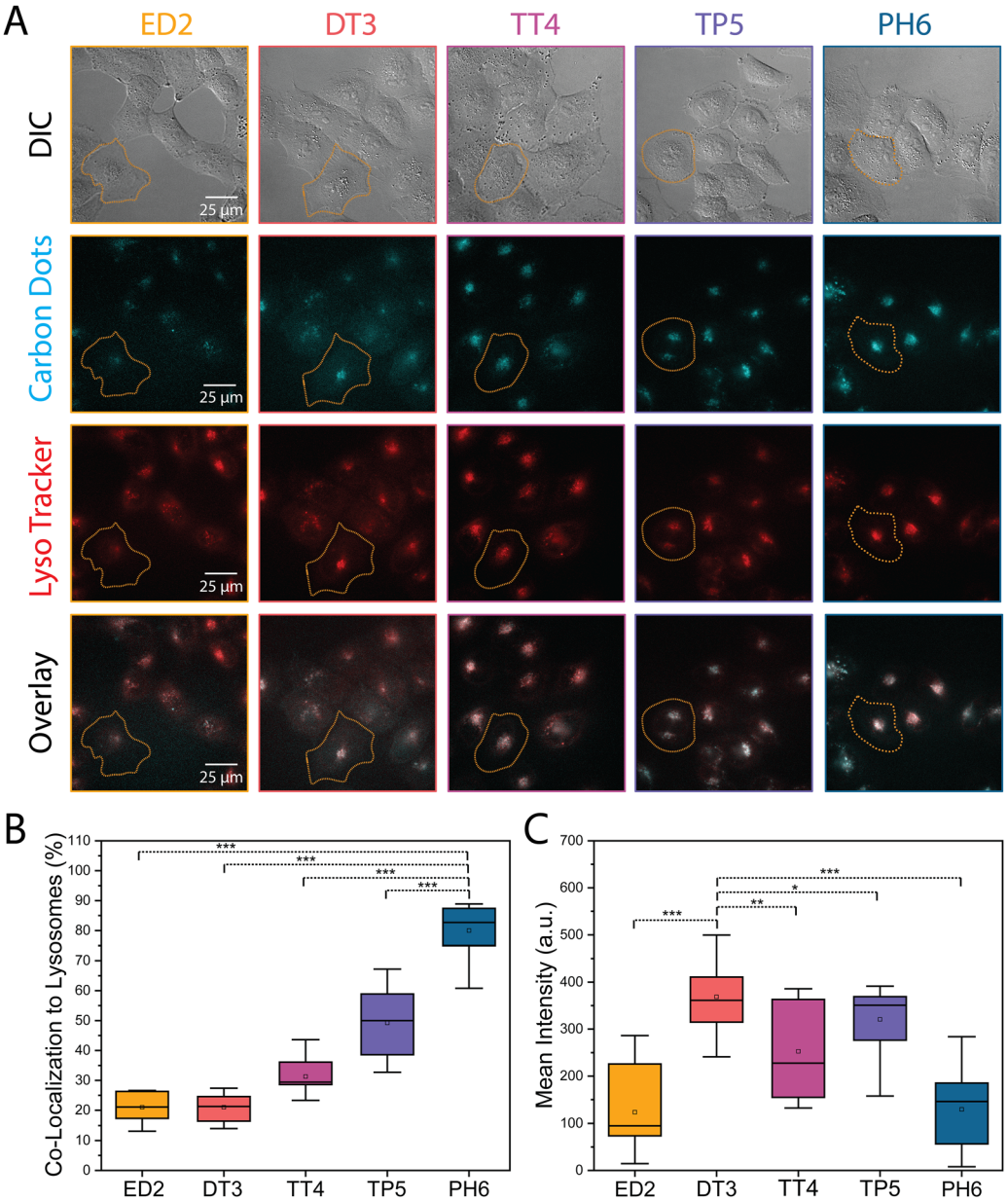

Fig. 5 CDs localize to the lysosomes and cytosol in HeLa cells. (A) Brightfield (top) and fluorescence images show live HeLa cells 24 hours after treatment with 1000 µg mL^{-1} of the CDs (blue) as indicated, co-stained for lysotracker (red). The scale bar is 25 µm. (B) A box and whiskers graph show the % co-localization of CDs as indicated with lysotracker using Pearson's correlation coefficient. Bars indicate standard deviation. One-way ANOVA and paired *t*-tests to PH6 were done to show significance (***$p < 0.001$). (C) A box and whiskers graph shows the mean intensity (a.u.) of CDs in the cytosol. Bars indicate standard deviation. A one-way ANOVA and paired *t*-tests to DT3 were done to show significance (*$p < 0.05$; **$p < 0.01$; ***$p < 0.001$).

uptake in both HFF-1 and HeLa cells positively correlated with surface charge, which increased with amine passivation. With increased passivation, surface carboxyl decreases while amines increase, resulting in an increase in positive surface charge. For example, PH6-CDs had the strongest cellular uptake and the most positive zeta-potential at +6 mV. It is not clear why surface charge would increase their uptake, but this could enhance electrostatic interactions with the negatively charged phospholipids in the cellular membrane to enrich them at sites of endocytic entry.[41] Additionally, studies have shown that the protein corona effect may also highly impact the uptake of CDs in different cells. Highly cationic CDs have been shown to have a protein corona that favours their cellular uptake, although this also increased their toxicity.[42] Thus, it is crucial to consider how modulating different physicochemical properties of CDs can mitigate their biological functions.

We also found that an increase in amine passivation is associated with increased localization to the lysosomes in HFF-1 and HeLa cells. Strikingly, 80% of PH6-CDs were localized to the lysosomes in HeLa cells, while 52% localized to

lysosomes in HFF-1 cells. This suggests that PH6-CDs could be developed for use as nanoprobes for the lysosomes, especially for cell types that share more similarities to HeLa cells. HeLa cells are epithelial in origin and cancerous *vs.* HFF-1, which are non-cancerous fibroblasts. As discussed previously, many endocytic pathways can be utilized by cells to uptake CDs. While both HeLa cells and HFF-1 cells can utilize similar endocytic pathways, the expression levels, or activities of proteins in these pathways may differ between the two cell types. These variations could potentially lead to differences in the efficiency or regulation of endocytosis, thus impacting their respective abilities to uptake CDs.[43–45]

Lastly, and unexpectedly, DT3-CDs were found to be highly enriched in the cytosol of HFF-1 and HeLa cells compared to the other CDs. These CDs were the most negative, and log*P* measurements revealed that they have amphiphilic properties that could permit them to passively enter cells. They could also escape the endosomes more easily compared to the other amine-passivated CDs, although it is not clear what property would permit them, but not the other CDs, to do this as they showed very similar optical and physicochemical properties. It is also possible that DT3-CDs form small aggregates that could affect how they escape endosomes, and/or could make them more visible in the cytosol. The ability of the DT3-CDs (or other CDs) to be cytosolic could make them useful for drug delivery, especially since many delivery systems have limited access to the cytosol where the drugs are needed for their mechanism of action.[46,47]

Conclusions

Different extents of amine-passivation generate CDs with distinct characteristics that could be advantageous for distinct bioimaging and drug delivery applications. PH6-CDs are very bright with high quantum yield and photostability with specificity for the lysosomes, making them ideal as bioimaging tools for lysosome-specific sensing applications. On the other hand, DT3-CDs may be well-suited for applications that require drug delivery to the cytosol. Very few nanoparticles have been shown to have the capacity to easily localize to the cytosol, since most are trapped in the endomembrane system making it challenging to deliver drugs with molecular targets that are cytosolic or in other organelles.

Our study also revealed differences in the distribution of the different amine-passivated CDs in HeLa *vs.* HFF-1 cells that reflect the distinct organization of the endomembrane system and mechanisms of uptake. For example, the lysosomes are more broadly distributed in HFF-1 cells, while they cluster near the nucleus of HeLa cells. Further, while PH6-CDs have a strong preference for the lysosomes in both cell types, there are proportionally more in the lysosomes of HeLa compared to HFF-1 cells. These findings reveal the need to gain more knowledge of how nanoparticles enter and localize in different cell types before considering their use for drug delivery or diagnostics. In addition, this knowledge could reveal some important differences in targeting cancer *vs.* non-cancer cells.

Author contributions

Conceptualization, Adryanne Clermont-Paquette and Rafik Naccache; funding acquisition, Alisa Piekny and Rafik Naccache; methodology, Adryanne Clermont-Paquette, Kevin Larocque, Alisa Piekny and Rafik Naccache; resources, Alisa Piekny and Rafik Naccache; writing – original draft, Adryanne Clermont-Paquette, Alisa Piekny and Rafik Naccache; writing – review & editing, Adryanne Clermont-Paquette, Kevin Larocque, Alisa Piekny and Rafik Naccache.

Conflicts of interest

There are no conflicts to declare.

Acknowledgements

The authors would like to acknowledge the funding sources for their financial support of this research. RN is grateful to NSERC for funding through the Discovery Grant. RN is also grateful to Concordia University for funding through the University Research Chair Program. AP is grateful to NSERC for funding through the Discovery Grant and Concordia University for funding through the University Research Chair Program. ACP thanks Concordia University for financial support. The TEM experiments were performed at the Centre for NanoScience Research at Concordia University with the help of Nooshin Movahed. XPS studies were performed at McGill University (MIAM Facilities in the Department of Mining and Materials Engineering) with the assistance of Lihong Shang. Microscopy was performed in the Centre for Microscopy and Cellular Imaging at Concordia University with the help of Dr Chris Law. Parts of some figures were created with BioRender.com.

Notes and references

1 F. R. Baptista, S. A. Belhout, S. Giordani and S. J. Quinn, Recent developments in carbon nanomaterial sensors, *Chem. Soc. Rev.*, 2015, **44**(13), 4433–4453.
2 D. Koltsov and I. Koltsov, Application of Nanomaterials to Industry: How are Nanomaterials Used and What Drives Future Applications?, *Metrol. Stand. Nanotechnol.*, 2017, 465–484.
3 Z. Li, L. Wang, Y. Li, Y. Feng and W. Feng, Frontiers in carbon dots: Design, properties and applications, *Mater. Chem. Front.*, 2019, **3**(12), 2571–2601.
4 R. R. Pandey and C. C. Chusuei, Carbon nanotubes, graphene, and carbon dots as electrochemical biosensing composites, *Molecules*, 2021, **26**(21), 26216674.
5 D. Janas, From bio to nano: A review of sustainable methods of synthesis of carbon nanotubes, *Sustainability*, 2020, **12**(10), 12104115.
6 N. Anzar, R. Hasan, M. Tyagi, N. Yadav and J. Narang, Carbon nanotube – A review on Synthesis, Properties and plethora of applications in the field of biomedical science, *Sensors Int.*, 2020, **1**, 100003.

7 C. Liao, Y. Li and S. C. Tjong, Graphene Nanomaterials: Synthesis, Biocompatibility, and Cytotoxicity, *Int. J. Mol. Sci.*, 2018, **19**, 35–64.
8 S. Shahriari, M. Sastry and S. Panjikar, Graphene and Graphene Oxide as a Support for Biomolecules in the Development of Biosensors, *Nanotechnol., Sci. Appl.*, 2021, **14**, 197–220, DOI: 10.2147/NSA.S334487.
9 X. Xu, R. Ray and Y. Gu, *et al.*, Electrophoretic analysis and purification of fluorescent single-walled carbon nanotube fragments, *J. Am. Chem. Soc.*, 2004, **126**(40), 12736–12737.
10 L. Cui, X. Ren, M. Sun, H. Liu and L. Xia, Carbon dots: Synthesis, properties and applications, *Nanomaterials*, 2021, **11**(12), 3419.
11 H. Li, X. Yan and D. Kong, *et al.*, Recent advances in carbon dots for bioimaging applications, *Nanoscale Horiz.*, 2020, **5**(2), 218–234.
12 M. L. Liu, B. B. Chen, C. M. Li and C. Z. Huang, Carbon dots: Synthesis, formation mechanism, fluorescence origin and sensing applications, *Green Chem.*, 2019, **21**(3), 449–471.
13 T. V. De Medeiros, J. Manioudakis, F. Noun, J. R. Macairan, F. Victoria and R. Naccache, Microwave-assisted synthesis of carbon dots and their applications, *J. Mater. Chem. C*, 2019, **7**(24), 7175–7195.
14 J. H. Liu, L. Cao and G. E. LeCroy, *et al.*, Carbon ''Quantum'' Dots for Fluorescence Labeling of Cells, *ACS Appl. Mater. Interfaces*, 2015, **7**(34), 19439–19445.
15 Q. Zhang, S. Xie and Y. Yang, *et al.*, A facile synthesis of highly nitrogen-doped carbon dots for imaging and detection in biological samples, *J. Anal. Methods Chem.*, 2018, **2018**, 7890937.
16 J. R. Macairan, T. V. de Medeiros, M. Gazzetto, F. Yarur Villanueva, A. Cannizzo and R. Naccache, Elucidating the mechanism of dual-fluorescence in carbon dots, *J. Colloid Interface Sci.*, 2022, **606**, 67–76.
17 B. Ju, Y. Wang and Y. M. Zhang, *et al.*, Photostable and Low-Toxic Yellow-Green Carbon Dots for Highly Selective Detection of Explosive 2,4,6-Trinitrophenol Based on the Dual Electron Transfer Mechanism, *ACS Appl. Mater. Interfaces*, 2018, **10**(15), 13040–13047.
18 S. M. Ng, *Carbon Dots as Optical Nanoprobes for Biosensors*, in *Nanobiosensors for Biomolecular Targeting*, ed. C. B. Subash and T. L. Gopinath, Elsevier Inc., 2019.
19 D. Xu, Q. Lin and H. T. Chang, Recent Advances and Sensing Applications of Carbon Dots, *Small Methods*, 2020, **4**(4), 1–17.
20 F. Du, J. Li and Y. Hua, *et al.*, Multicolor nitrogen-doped carbon dots for live cell imaging, *J. Biomed. Nanotechnol.*, 2015, **11**(5), 780–788.
21 S. T. Yang, X. Wang and H. Wang, *et al.*, Carbon dots as nontoxic and high-performance fluorescence imaging agents, *J. Phys. Chem. C*, 2009, **113**(42), 18110–18114.
22 L. Thoo, M. Z. Fahmi, I. N. Zulkipli, N. Keasberry and A. Idris, Interaction and cellular uptake of surface-modified carbon dot nanoparticles by J774.1 macrophages, *Cent. Eur. J. Immunol.*, 2017, **42**(3), 324–330.
23 P. Koutsogiannis, E. Thomou, H. Stamatis, D. Gournis and P. Rudolf, Advances in fluorescent carbon dots for biomedical applications, *Adv. Phys.: X*, 2020, **5**(1), 1758592.
24 A. Panariti, G. Miserocchi and I. Rivolta, The effect of nanoparticle uptake on cellular behavior: Disrupting or enabling functions?, *Nanotechnol., Sci. Appl.*, 2012, **5**(1), 87–100.
25 A. Truskewycz, H. Yin, N. Halberg, D. T. H. Lai, A. S. Ball, V. K. Truong, A. M. Rybicka and I. Cole, *et al.*, Carbon Dot Therapeutic Platforms: Administration, Distribution, Metabolism, Excretion, Toxicity, and Therapeutic Potential, *Small*, 2022, **18**(16), 2106342.
26 , Selective photothermal killing of cancer cells using LED-activated nucleus targeting fluorescent carbon dots, *Nanoscale Adv.*, 2019, **1**(8), 2840–2846.
27 W. Lu, X. Gong, M. Nan, Y. Liu, S. Shuang and C. Dong, Comparative study for N and S doped carbon dots: Synthesis, characterization and applications for Fe3+ probe and cellular imaging, *Anal. Chim. Acta*, 2015, **898**, 116–127.
28 A. Sachdev, I. Matai and P. Gopinath, Implications of surface passivation on physicochemical and bioimaging properties of carbon dots, *RSC Adv.*, 2014, **4**(40), 20915–20921.
29 L. Pan, S. Sun and A. Zhang, *et al.*, Truly Fluorescent Excitation-Dependent Carbon Dots and Their Applications in Multicolor Cellular Imaging and Multidimensional Sensing, *Adv. Mater.*, 2015, 7782–7787.
30 J. R. Macairan, D. B. Jaunky, A. Piekny and R. Naccache, Intracellular ratiometric temperature sensing using fluorescent carbon dots, *Nanoscale Adv.*, 2019, **1**(1), 105–113.
31 H. Ali, S. Ghosh and N. R. Jana, Fluorescent carbon dots as intracellular imaging probes, *Wiley Interdiscip. Rev.: Nanomed. Nanobiotechnol.*, 2020, **12**(4), 1–15.
32 J. R. Macairan, I. Zhang, A. Clermont-Paquette, R. Naccache and D. Maysinger, Ratiometric pH Sensing in Living Cells Using Carbon Dots, *Part. Part. Syst. Charact.*, 2020, **1900430**, 1–7.
33 M. Havrdova, K. Hola and J. Skopalik, *et al.*, Toxicity of carbon dots-Effect of surface functionalization on the cell viability, reactive oxygen species generation and cell cycle, *Carbon*, 2016, **99**, 238–248.
34 D. Hühn, K. Kantner and C. Geidel, *et al.*, Polymer-coated nanoparticles interacting with proteins and cells: Focusing on the sign of the net charge, *ACS Nano*, 2013, **7**(4), 3253–3263.
35 M. Danaei, M. Dehghankhold and S. Ataei, *et al.*, Impact of particle size and polydispersity index on the clinical applications of lipidic nanocarrier systems, *Pharmaceutics*, 2018, **10**(2), 1–17.
36 N. Zhou, S. Zhu and S. Maharjan, *et al.*, Elucidating the endocytosis, intracellular trafficking, and exocytosis of carbon dots in neural cells, *RSC Adv.*, 2014, **4**(107), 62086–62095.
37 D. Manzanares and V. Ceña, Endocytosis: The nanoparticle and submicron nanocompounds gateway into the cell, *Pharmaceutics*, 2020, **12**(4), 1–22.
38 S. E. A. Gratton, P. A. Ropp and P. D. Pohlhaus, *et al.*, The effect of particle design on cellular internalization pathways, *Proc. Natl. Acad. Sci. U. S. A.*, 2008, **105**(33), 11613–11618.

39 J. Zhang and S. H. Yu, Carbon dots: large-scale synthesis, sensing and bioimaging, *Mater. Today*, 2016, **19**(7), 382–393.
40 S. K. Bhal, Log P—Making Sense of the Value, *Adv. Chem. Dev.*, 2007, 1–4.
41 Z. Hallaji, Z. Bagheri, M. Oroujlo, M. Nemati, Z. Tavassoli and B. Ranjbar, An insight into the potentials of carbon dots for in vitro live-cell imaging: recent progress, challenges, and prospects, *Microchim. Acta*, 2022, **189**(5), 190–210.
42 Y. Arezki, F. Delalande and C. Schaeffer-Reiss, *et al.*, Surface charge influences protein corona, cell uptake and biological effects of carbon dots, *Nanoscale*, 2022, **14**(39), 14695–14710.
43 D. Beaudet, S. Badilescu and K. Kuruvinashetti, *et al.*, Comparative study on cellular entry of incinerated ancient gold particles (Swarna Bhasma) and chemically synthesized gold particles, *Sci. Rep.*, 2017, **7**, 10678.
44 J. J. Rennick, A. P. R. Johnston and R. G. Parton, Key principles and methods for studying the endocytosis of biological and nanoparticle therapeutics, *Nat. Nanotechnol.*, 2021, **16**(3), 266–276.
45 G. Sahay, D. Y. Alakhova and A. V. Kabanov, Endocytosis of nanomedicines, *J. Controlled Release*, 2010, **145**(3), 182–195.
46 H. Son, J. Shin and J. Park, Recent progress in nanomedicine-mediated cytosolic delivery, *RSC Adv.*, 2023, **13**(15), 9788–9799.
47 H. J. Wang, X. He, T. Y. Luo, J. Zhang, Y. H. Liu and X. Q. Yu, Amphiphilic carbon dots as versatile vectors for nucleic acid and drug delivery, *Nanoscale*, 2017, **9**(18), 5935–5947.